PNAS RESEARCH ARTICLE | APPLIED BIOLOGICAL SCIENCES ENGINEERING

Multiscale embedded printing of engineered human tissue and organ equivalents

Cheng Zhang[a,b,1], Weijian Hua[a,1], Kellen Mitchell[a], Lily Raymond[a], Fatemeh Delzendehrooy[c], Lai Wen[d], Changwoo Do[e], Jihua Chen[f], Ying Yang[g], Gabe Linke[h], Zhengyi Zhang[i], Mena Asha Krishnan[i], Mitchell Kuss[i], Ryan Coulter[a], Erick Bandala[a], Yiliang Liao[c,2], Bin Duan[i,2], Danyang Zhao[b,2], Guangrui Chai[k,2], and Yifei Jin[a,2]

Edited by Lijie Grace Zhang, The George Washington University, Washington, DC; received August 10, 2023; accepted January 9, 2024 by Editorial Board Member Yonggang Huang

Creating tissue and organ equivalents with intricate architectures and multiscale functional feature sizes is the first step toward the reconstruction of transplantable human tissues and organs. Existing embedded ink writing approaches are limited by achievable feature sizes ranging from hundreds of microns to tens of millimeters, which hinders their ability to accurately duplicate structures found in various human tissues and organs. In this study, a multiscale embedded printing (MSEP) strategy is developed, in which a stimuli-responsive yield-stress fluid is applied to facilitate the printing process. A dynamic layer height control method is developed to print the cornea with a smooth surface on the order of microns, which can effectively overcome the layered morphology in conventional extrusion-based three-dimensional bioprinting methods. Since the support bath is sensitive to temperature change, it can be easily removed after printing by tuning the ambient temperature, which facilitates the fabrication of human eyeballs with optic nerves and aortic heart valves with overhanging leaflets on the order of a few millimeters. The thermosensitivity of the support bath also enables the reconstruction of the full-scale human heart on the order of tens of centimeters by on-demand adding support bath materials during printing. The proposed MSEP demonstrates broader printable functional feature sizes ranging from microns to centimeters, providing a viable and reliable technical solution for tissue and organ printing in the future.

3D bioprinting | multiple scales | high-precision | human tissue and organ equivalents | yield-stress support bath

Significance

A multiscale embedded printing strategy is developed which is capable of reconstructing engineered human tissue and organ equivalents with functional feature sizes on the orders from microns to tens of centimeters. A dynamic layer height control method is proposed to print a cornea structure with a smooth surface. Both homogenous and heterogeneous human eyeball equivalents and aortic heart valve construct are successfully fabricated in a yield-stress support bath which can be liquefied at 4 °C. Finally, a full-scale human heart structure is printed using a short dispensing nozzle by on-demand adding support bath material during printing.

Reconstructing human tissues and organs from an autologous source is one of the ultimate goals of tissue engineering (1, 2). Engineered tissue and organ equivalents can not only be used as transplants to overcome the crisis of global organ shortage (3, 4) but also present diverse promising biomedical applications, such as surgery planning (5), education (6), and disease modeling (7), to name a few.

The conventional strategy in tissue engineering for reconstructing tissues and organs is to seed living cells onto a scaffold made from either biomaterials (8, 9) or decellularized natural organs (10, 11). However, it is still challenging to rebuild human tissues and organs with complex architectures, heterogeneous cell and tissue constituents, as well as sophisticated physiological functions using this strategy. The emergence of three-dimensional (3D) bioprinting provides a promising technical solution that can accurately position various biomaterials and cells in a layer-by-layer fashion based on a patient-specific design. Of the three commonly used bioprinting strategies [inkjet-based (12, 13), extrusion-based (14, 15), and light-based (16)], extrusion-based 3D bioprinting has evoked the majority of interest because of its broad range of printable materials, low fabrication cost, and capability of depositing multiple cells/bioinks (17, 18). Particularly, embedded ink writing, a subtechnique of extrusion-based 3D bioprinting, has been proposed in recent years, in which a bioink is deposited into a predefined architecture within a support bath usually made from a yield-stress fluid. The bath is switchable between liquid and solid-like states during printing and provides stable and ubiquitous physical supports, demonstrating great potential for fabricating engineered tissue and organ equivalents with intricate structures (19, 20).

Human tissues and organs generally possess functional feature sizes at multiple scales (Fig. 1*A*). For example, the cornea is a transparent layer on the front of a human eyeball with a surface roughness on the order of submicrons (21, 22). An eyeball and aortic heart valve have an overall size of around tens of millimeters, but the key features [e.g., the diameter of the optic nerve sheath (23) and thickness of the leaflet (24)] are on the order of a few millimeters. The heart is one of the largest organs in the human body, which has a whole size of more than ten centimeters (25). Although significant success has been achieved in tissue/organ printing using current embedded ink writing approaches [such as freeform reversible embedding of suspended

Author contributions: C.Z., W.H., Y.L., B.D., G.C., and Y.J. designed research; C.Z., W.H., K.M., L.R., F.D., C.D., J.C., G.L., M.A.K., M.K., R.C., and E.B. performed research; C.Z., W.H., L.W., C.D., J.C., Y.Y., and Z.Z. analyzed data; Y.L., B.D., D.Z., G.C., and Y.J. supervised project; and C.Z., W.H., Z.Z., R.C., E.B., B.D., D.Z., G.C., and Y.J. wrote the paper.

The authors declare no competing interest.

This article is a PNAS Direct Submission. L.G.Z. is a guest editor invited by the Editorial Board.

[1]C.Z. and W.H. contributed equally to this work.

[2]To whom correspondence may be addressed. Email: leonl@iastate.edu, bin.duan@unmc.edu, zhaody@dlut.edu.cn, chaigr@sj-hospital.org, or yifeij@unr.edu.

This article contains supporting information online at https://www.pnas.org/lookup/suppl/doi:10.1073/pnas.2313464121/-/DCSupplemental.

Published February 12, 2024.

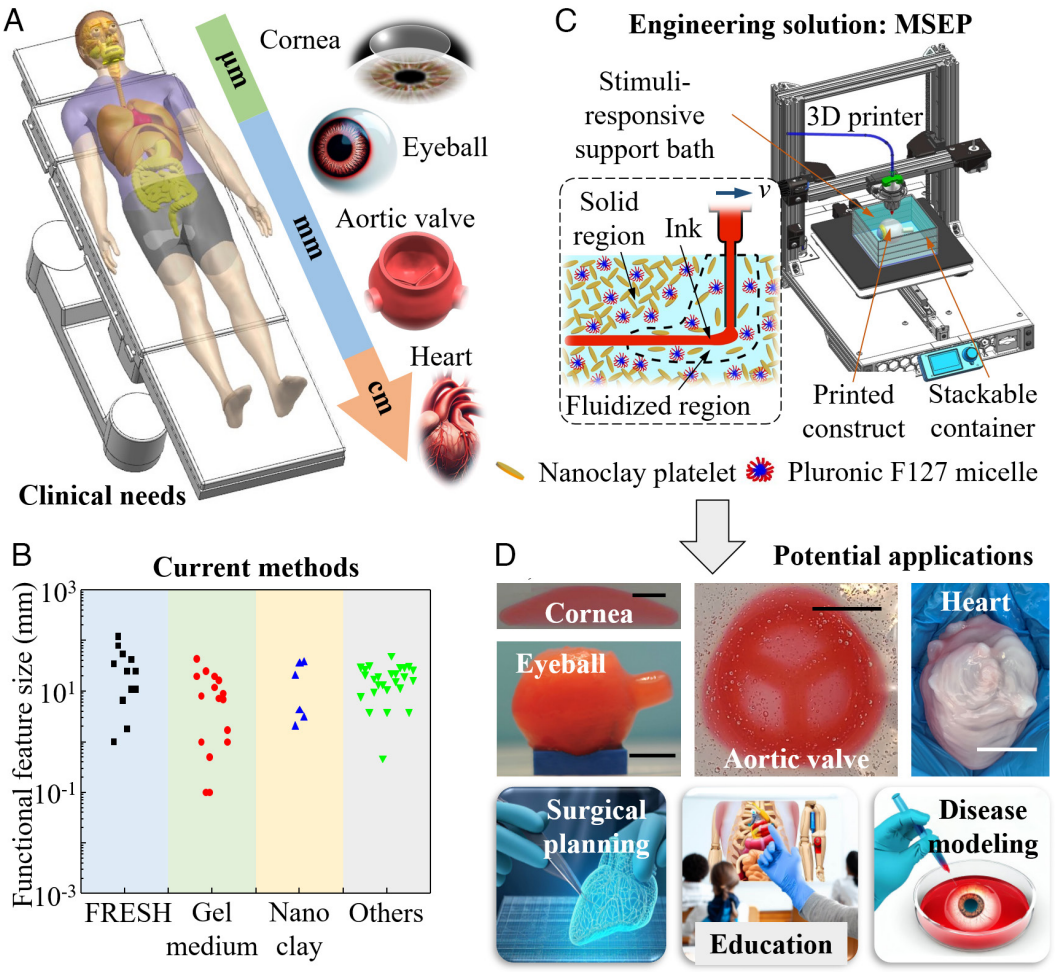

Fig. 1. Schematic of printing human tissues and organs with multiscale functional feature sizes using the proposed MSEP method. (*A*) Clinical needs of reconstructing engineered human tissues and organs with multiscale functional feature sizes. (*B*) Size constraint of existing embedded ink writing approaches. (*C*) Schematic of the proposed MSEP method, in which engineered human tissues and organs are printed in a stimuli-responsive yield-stress support bath using a short dispensing nozzle. (*D*) Targeted tissue and organ equivalents and their potential applications. (Scale bars, 2.0 mm for the cornea, 10.0 mm for the eyeball and aortic valve, and 30.0 mm for the heart.)

hydrogel (FRESH) (1, 26–30), writing in granular gel medium (4, 8, 15, 31–35), nanoclay-assisted 3D printing (3, 14, 36), and others (7, 10, 18–20, 37–44)], the achievable feature sizes are still constrained on the orders of hundreds of microns to tens of millimeters, as summarized in Fig. 1*B*. This limitation is mainly attributed to the poor flowability of current yield-stress fluids (as summarized in *SI Appendix*, Table S1), making it difficult to add support bath materials on demand during printing. As a result, the overall size and resolution of a printable construct are directly limited by the geometries (i.e., length and inner diameter) of the available dispensing nozzle, bioink viscosity, and cell density. To accurately duplicate human tissues and organs with multiscale key features, it is necessary to develop alternative embedded ink writing strategies.

Results and Discussion

Multiscale Embedded Printing and Potential Application Scope. In this work, a multiscale embedded printing (MSEP) approach is explored and evaluated for its effectiveness in producing engineered tissue and organ equivalents with enhanced precision and accuracy. As shown in Fig. 1*C*, the support bath material used in this approach is a stimuli-responsive yield-stress fluid, which is composed of a thermosensitive polymer component—Pluronic F127 and a yield-stress additive component—nanoclay platelets. Pluronic F127 is a triblock copolymer that consists of poly(ethylene oxide) (PEO) and poly(propylene oxide) (PPO) blocks. When the working temperature is higher than a threshold temperature, known as critical micelle temperature (T_{cm}), the hydrophobic PPO block is surrounded by hydrophilic PEO blocks in a spherical micelle morphology. Numerous jammed micelles enable Pluronic F127 to present a gel state at the macroscale level (*Inset* of Fig. 1*C*). When the working temperature is lower than T_{cm}, the hydrophobic PPO core is hydrated, which makes PEO and PPO blocks soluble in an aqueous solvent in an alternating linear PEO–PPO–PEO configuration. At the macroscopic view, Pluronic F127 converts from a gel state to a sol state with low viscosity. Nanoclay is a class of 2D nanoparticles with positive and negative charges on the edge and faces, respectively (*Inset* of Fig. 1*C*). In an aqueous solvent, nanoclay platelets aggregate together due to electrostatic interactions, forming a "house-of-cards" microstructure. When an external shear stress higher than the nanoclay suspension's yield stress is applied, this house-of-cards microstructure is disrupted, allowing suspension to transition into a liquid state. Once the external stress is removed or reduced below the yield stress, the disrupted microstructure can rapidly rebuild, causing the suspension to exhibit solid-like behavior. Upon mixing, the resulting nanoclay-Pluronic F127 nanocomposite acquires the thermosensitivity and yield-stress property of its individual components.

When serving as a support bath, the movement of the nozzle induces shear stress, creating a fluidized region around the nozzle tip that facilitates ink deposition within the bath. The nanocomposite

far away from the nozzle experiences shear stress lower than the yield stress, resulting in the formation of a solid region that stably holds a printed structure in situ. In addition, due to the thermosensitivity, sol-state support bath material can be easily added to a stackable container at lower temperatures because of its negligible yield stress, low viscosity, and good flowability. When the temperature of the newly added support bath rises to the ambient temperature (45), the printing process can be continued, as shown in Fig. 1*C*. Thus, it is technically feasible to achieve the fabrication of multiscale human tissues and organs using a short dispensing nozzle with a small orifice to ensure the resolution and cell viability, if printed. In this study, four representative tissue and organ equivalents, including the cornea, eyeball, aortic heart valve, and full-scale human heart, are reconstructed via MSEP to demonstrate the printing capability space of the proposed approach, as shown in Fig. 1*D*.

Characterization of the Support Bath Material. In MSEP, the support bath material must have a sufficient yield stress at room temperature to effectively hold the deposited features in place within the bath. Herein, the effects of Pluronic F127 concentration on yield stress are investigated, and the results are illustrated in Fig. 2*A*. It is observed that at three representative concentrations, nanoclay-Pluronic F127 nanocomposites present different rheological behaviors. When the Pluronic F127 concentration is at a low level [e.g., 0.25% (w/v)], the nanocomposite possesses a low yield stress of 0.72 Pa. When Pluronic F127 is added at a medium concentration, e.g., 5% (w/v), the resulting nanocomposite loses its yield-stress property and behaves as a shear-thinning suspension. In contrast, when the Pluronic F127 concentration reaches a high level [e.g., 30% (w/v)], the nanocomposite becomes a yield-stress fluid with a yield stress of 380.50 Pa, significantly higher than the sum of the yield stress of each component (45). This phenomenon is attributed to the interactions between nanoclay platelets and Pluronic F127 polymer chains, as well as the formed microstructures at different concentrations. Micellization of Pluronic F127 is not only determined by ambient temperature but also depends on its concentration (46). When the concentration [e.g., 0.25% (w/v)] is below a critical value [usually 20% (w/v) (47)], linear PEO-PPO-PEO chains, instead of micelles, mainly exist in the nanocomposite. Specifically, PPO blocks act as anchors to be absorbed onto nanoclay platelets since hydrophobic PPO blocks have a better affinity with nanoclay in the aqueous solvent (48, 49). As a result, a less densified house-of-cards microstructure is formed, causing the yield stress of the resulting nanocomposite (0.72 Pa) to be lower than that of pure nanoclay at 2% (w/v) [13.6 Pa (45)]. When the Pluronic F127 concentration increases to 5% (w/v), there are more PEO–PPO–PEO chains to encapsulate all nanoclay platelets and prevent the formation of house-of-cards microstructure. As a result, the

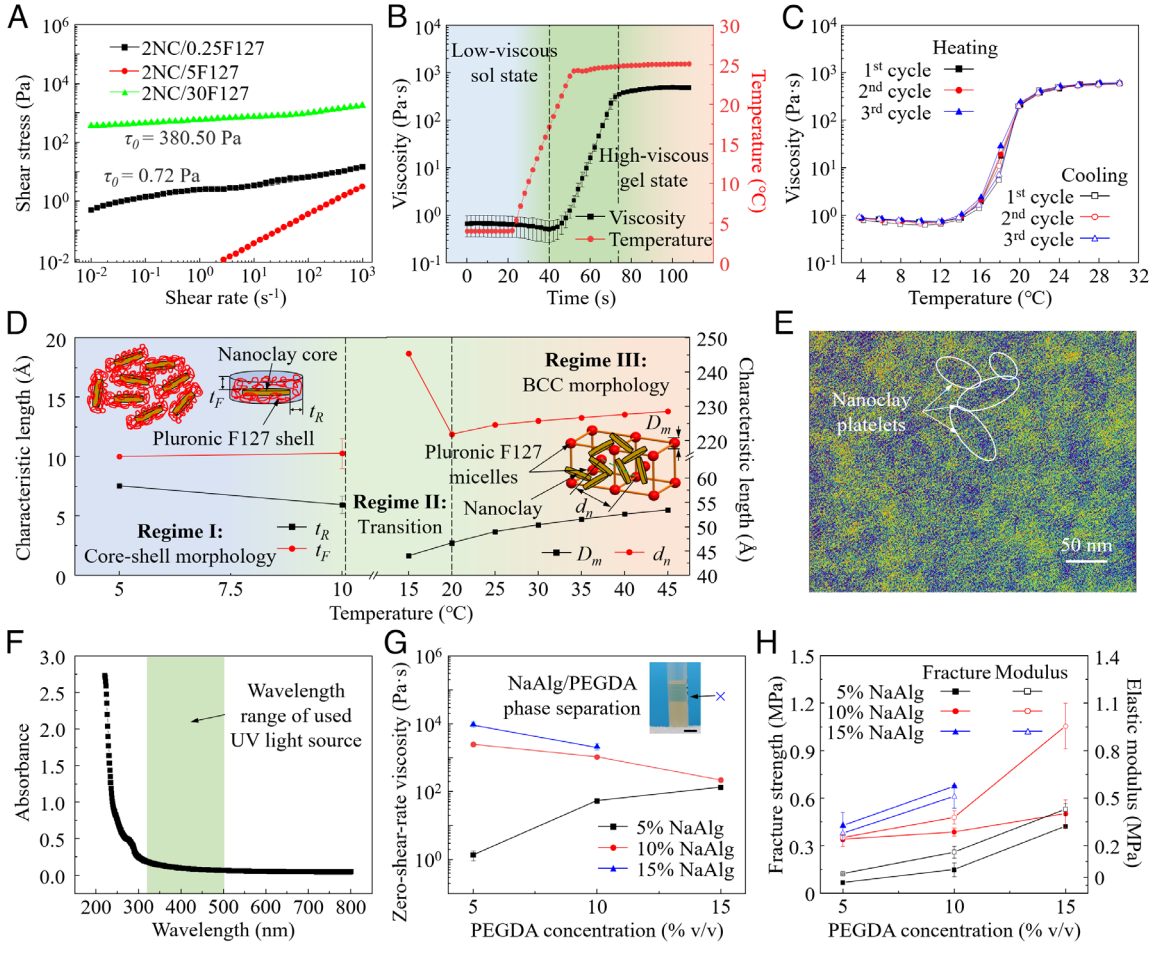

Fig. 2. Characterization of support bath materials and ink materials. (*A*) Yield stresses of nanocomposites with 2% (w/v) nanoclay (NC) and 0.25, 5, and 30% (w/v) Pluronic F127 (F127). (*B*) Thermosensitivity of the nanocomposite with 2% (w/v) nanoclay and 30% (w/v) Pluronic F127. (*C*) Repeatable thermosensitivity in multiple heating-cooling cycles. (*D*) Microstructure evolution in the temperature range of 5 to 45 °C (t_F: face thickness, t_R: rim thickness, D_m: micelle diameter, and d_n: nearest neighbor distance). (*E*) TEM image of nanoclay distribution within the nanocomposite. (*F*) UV transparency of the nanocomposite. (*G*) Printability of bioinks with different formulas. (Scale bar, 1.0 cm). (*H*) Mechanical properties of bioinks with different formulas. The quantitative values in *A*, *B*, *D*, *G*, and *H* are reported as means ± SD with n = 3 samples per group.

nanocomposite turns into a shear-thinning fluid. At a concentration higher than the critical value [e.g., 30% (w/v)], Pluronic F127 forms a jammed micelle microstructure while released nanoclay platelets rebuild the house-of-cards microstructure. The coexistence of dual microstructures enables the nanocomposite to possess a high yield stress of 380.50 Pa, which is suitable for MSEP applications. Therefore, the nanocomposite with this formula [i.e., 2% (w/v) nanoclay and 30% (w/v) Pluronic F127] is selected as the thermosensitive yield-stress support bath.

In order to add support bath materials during printing, the nanocomposite for MSEP must exhibit varying viscosities at different temperatures. Fig. 2*B* illustrates the viscosity change over time and temperature. At 5 °C, the nanocomposite possesses a low zero-shear-rate viscosity less than 1.0 Pa·s. This viscosity is comparable to or even lower than that of materials commonly processed by casting, e.g., polydimethylsiloxane with a viscosity of around 3.5 Pa·s (50, 51). As a result, the good flowability at lower temperatures can ensure the rapid filling of containers when perfusing additional support bath materials in printing. When the temperature increases to 20 °C, the nanocomposite's viscosity starts to increase and stabilizes at a relatively high level of more than 10^3 Pa·s at room temperature, indicating that the nanocomposite switches to a yield-stress fluid and is suitable to serve as a support bath. The viscosity change is reversible and repeatable. As shown in Fig. 2*C*, the nanocomposite demonstrates stable viscosities at lower and higher temperatures in three heating-cooling cycles, making it feasible to liquefy the support bath after printing for easily releasing a printed construct.

The change of macroscopic rheological behaviors upon temperature variation can be explained by the evolution of the nanocomposite's microstructure. Small angle neutron scattering (SANS) is applied to obtain the microstructures at different temperatures (*SI Appendix*, Fig. S1), and the results are summarized in Fig. 2*D*. In a low-temperature range (from 5 to 10 °C), Pluronic F127 exists in the nanocomposite in the form of linear PEO–PPO–PEO chains. The attachment of PPO blocks to nanoclay platelets enables nanoclay to be encapsulated by Pluronic F127, resulting in the formation of a core–shell microstructure within the nanocomposite, as shown in the *Inset* of Fig. 2*D*. Since nanoclay platelets are isolated from each other by Pluronic F127 shells, the house-of-cards microstructure cannot form, preventing the nanocomposite from possessing a high yield stress in this temperature range. The interaction distances between nanoclay platelets and Pluronic F127 molecules [including face thickness (t_F) and rim thickness (t_R) in Fig. 2*D*] can be calculated based on the SANS data by Eqs. (**1**– **3**) (48, 52) as follows:

$$I(Q) = B_{inc} + \frac{\phi_p}{v_p}\int_0^{R_p=\infty} n(R_0, R_p, \sigma_0)P(Q, R_p, H_p, t_R, t_F, \rho_p, \rho_l, \rho_s)\, dR_p, \quad [1]$$

$$n(R_0, R_p, \sigma_0) = \frac{exp\left[-\frac{1}{2}\left(\frac{lnR_0 - lnR_p}{\sigma_0} - \frac{1}{2}\sigma_0\right)^2\right]}{(2\pi)^{1/2}\sigma_0 R_p}, \quad [2]$$

$$P(Q) = \int_0^{\pi/2} sin\theta \cdot \left\{ v_t(\rho_l - \rho_s)\frac{sin\left[Q(H_p + 2t_F)(cos\theta)/2\right]}{Q(H_p + 2t_F)(cos\theta)/2}\frac{2J_1\left[Q(R_p + 2t_R)sin\theta\right]}{Q(R_p + 2t_R)sin\theta} + v_p(\rho_p - \rho_l)\frac{sin\left[QH_p(cos\theta)/2\right]}{QH_p(cos\theta)/2}\frac{2J_1\left[QR_p sin\theta\right]}{QR_p sin\theta} \right\}^2 d\theta, \quad [3]$$

where B_{inc} is the scattering contribution from an incoherent background, ϕ_p is the volume fraction of particles, v_p is the volume of a single core particle, R_0 is the mean radius, R_p is the radius of the core, σ_0 is the mean SD, Q is the scattering vector, H_p is the thickness of the core, ρ_p is the scattering length density of the core, ρ_l is the scattering length density of the shell, ρ_s is the scattering length density of the solvent, v_t is the total volume of a core-shell unit, θ is the angle between the axis of a nanoclay platelet and the scattering vector, and J_1 is the first-order spherical Bessel function. The values of the parameters for fitting the SANS data are summarized in *SI Appendix*, Table S2. The results show that the temperature change from 5 to 10 °C leads to negligible variations in both t_F and t_R. Therefore, the microstructure of the nanocomposite is not varied significantly, which explains the stable rheological behaviors in Fig. 2 *B* and *C*. However, when the temperature increases from 15 to 45 °C, the nanocomposite's microstructure varies greatly. Pluronic F127 micelles generate and aggregate together to form the jammed micelle microstructure belonging to the polymer phase, while the detachment of PEO–PPO–PEO chains from nanoclay platelets results in the reconstruction of the house-of-cards microstructure belonging to the additive phase. Specifically, the house-of-cards microstructure interpenetrates with the jammed micelles to form an interactive dual microstructure in a body-centered cubic (BCC) morphology (*Inset* of Fig. 2*D*), which enables the nanocomposite to have a high yield stress, as measured in Fig. 2*A*. The key dimensions, including micelle radius ($R_m = D_m/2$) and nearest neighbor distance (d_n), can be determined according to the SANS data using Eqs. **4** and **5** as follows:

$$I(Q) = \frac{scale}{V_p}V_{lattice}P(Q)Z(Q), \quad [4]$$

$$V_{lattice} = \frac{16\pi}{3}\frac{R_m^3}{(d_n\sqrt{2})^3}, \quad [5]$$

where *scale* is the volume fraction of the micelles, V_p is the volume of the primary particles, and $V_{lattice}$ is the volume correction for the crystal structure. $P(Q)$ and $Z(Q)$ are the form factor of the normalized spheres and the paracrystalline structure factor for a BCC structure, respectively, which can be determined by the published results (53, 54). It is found that in the transition regime, d_n decreases rapidly and R_m increases slowly, which illustrates the micellization and jamming processes at temperatures between 10 and 20 °C. From 20 to 45 °C, d_n increases due to the rise of R_m because larger micelles also widen the distance between neighboring micelle lattices. The house-of-cards microstructure of nanoclay platelets is also imaged by transmission electron microscopy (TEM) at room temperature, as shown in Fig. 2*E*.

When printing ultraviolet (UV) cross-linkable bioinks, such as polyethylene glycol diacrylate (PEGDA) and gelatin-methacryloyl (GelMA), the support bath material must have good UV transparency such that sufficient radiation can reach the printed structure and cause photocross-linking. The transparency of the nanocomposite is

characterized, and the result is illustrated in Fig. 2*F*. In the UV wavelength range from 325 to 500 nm, the nanocomposite presents negligible absorbance. As a result, it can serve as an exceptional support bath for reconstructing human tissue and organ equivalents from UV-curable materials.

Determination of Bioink. In this study, a sodium alginate (NaAlg)/PEGDA mixture is selected as a photocurable bioink to print different human tissue and organ equivalents. The key rheological properties, including viscosity and shear moduli, of the mixtures with varying component concentrations are measured as shown in *SI Appendix*, Fig. S2*A*–*F*. The results are summarized in Fig. 2*G*. It is found that at a lower NaAlg concentration [e.g., 5% (w/v)], the increase of PEGDA concentration leads to the increase of zero-shear-rate viscosity from ~1.0 to 100.0 Pa·s. In contrast, when the NaAlg concentration exceeds a given value [e.g., 10% (w/v)], the viscosity decreases with the increase of PEGDA concentration. Particularly, phase separation is observed when the mixture has a NaAlg concentration of 15% (w/v) and a PEGDA concentration of 15% (v/v). This phenomenon is mainly attributed to the interactions between NaAlg and PEGDA. At 5% (w/v), alginate molecular chains are far apart from each other, resulting in weak intermolecular forces. In this case, the introduction of PEGDA enhances the end-binding effects (55) on alginate molecular chains through promoted interactions between PEGDA and NaAlg, thereby increasing the bioink viscosity. At higher NaAlg concentrations, intermolecular distance is compact, which makes the bioink more viscous. However, the addition of PEGDA enlarges the spacing between alginate molecules, weakening the entanglement between polymer chains and reducing the viscosity accordingly (56).

For clinical applications, printed equivalents need to have mechanical properties comparable to human tissues and organs. Thus, fracture strength and elastic modulus of each NaAlg/PEGDA mixture are characterized as shown in Fig. 2*H*. At a given PEGDA concentration [e.g., 10% (v/v)], the increase of NaAlg concentration from 5 to 15% (w/v) results in the raise of both the elastic modulus from 0.16 to 0.51 MPa and fracture strength from 0.15 to 0.68 MPa. At a given NaAlg concentration [e.g., 10% (w/v)], increasing the PEGDA concentration also increases both the elastic modulus and fracture strength. This is because more hydrogels in the mixture cause the formation of a more densified networked microstructure after cross-linking, which also enhances the mechanical properties (55, 57). Since some of the mixtures present elastic moduli fitting into the range of human soft tissues [from 1.0 kPa to 1.0 MPa (58)], they can be used for fabricating tissue and organ equivalents. Therefore, by comprehensively evaluating the rheological and mechanical properties (*SI Appendix*, Fig. S2*G*), the mixture with 10% (w/v) NaAlg and 15% (v/v) PEGDA is selected as the bioink for MSEP.

The degradation property of bioink is characterized in 13 d, as shown in *SI Appendix*, Fig. S3*A*. In the first 3 d, the bioink specimen rapidly loses 8.54% of its original mass, while in the following 10 d, the mass loss rate becomes stable. This degradation process is attributed to different cross-linking mechanisms of the bioink. NaAlg is a physically cross-linkable hydrogel, which has a weaker networked microstructure after cross-linking via calcium ions (59). Thus, when submerged in a phosphate-buffered saline (PBS) solution, the phosphate component in PBS de-cross-links the formed calcium alginate network by taking away calcium ions (60), resulting in the generation of free-moving alginate chains (61). The diffusion of alginate from the specimen leads to the mass loss eventually. In contrast, the networked microstructure of PEGDA formed via chemical cross-linking is more stable and irreversible. As a result, the bioink specimen can maintain its shape and a relatively constant mass after 3 d (62). The alginate diffusion also affects the mechanical properties of bioink. As demonstrated in *SI Appendix*, Fig. S3*B*, the specimen, before undergoing degradation, has an elastic modulus of 904.70 kPa. After immersing in the PBS for 3 d, the elastic modulus decreases greatly to 179.89 kPa, even lower than that of pure PEGDA (311.13 kPa). This is because NaAlg and PEGDA form an interpenetrating polymer network in the bioink specimen. The diffusion of alginate makes the network less densified than that of pure PEGDA, causing the weakened mechanical properties. From the cell growth aspect, bioinks with lower stiffness can facilitate the maintenance of the physiological phenotype of living cells (63, 64). Also, the elastic modulus of the specimen after degradation/dissociation still falls in the range of human soft tissues. Thus, the bioink designed in this work is suitable for fabricating human tissue and organ equivalents. The ratio of PEGDA in the bioink can be adjusted if more robust bioinks are needed, as shown in *SI Appendix*, Fig. S3*A*. With the increase of the PEGDA ratio, the mass loss decreases significantly in 14 d.

3D Printing of High-Precision Corneas. In extrusion-based 3D bioprinting, a construct is stacked layer by layer, resulting in the formation of layered surface morphology that is directly affected by the distance between adjacent layers, also known as layer height. As a result, it is challenging to fabricate engineered human tissues and organs with a surface roughness on the order of microns or below. In this work, a dynamic layer height control strategy is introduced, which can effectively eliminate the layered surface morphology to achieve high-precision constructs in MSEP.

In current extrusion-based 3D printing, layer height (d_s) along the vertical direction is constant, as illustrated in Fig. 3 *A*-1. However, surface roughness is directly determined by the inter-layer distance (d_f), instead of d_s, as shown in Fig. 3 *A*-2. Thus, when printing a 3D structure with an inclined angle (α), d_f varies with α as: $d_f = d_s / \sin\alpha$. As demonstrated in Fig. 3 *B*-1, d_f is doubled as α decreases from 90° to 30° if d_s is constant, which results in a deteriorated surface morphology. In the proposed strategy, d_f is controlled as a constant while d_s is dynamically adjusted as a function of α. Thus, the surface morphology is independent on the change of α, as shown in Fig. 3 *B*-2. The total surface roughness (R_t) and wall thickness (t) of inclined tubes in Fig. 3*B* are further quantified in Fig. 3*C*. For the constant layer height control, R_t decreases from 168.16 to 65.63 μm when α increases from 30° to 90° while t increases slightly from 0.50 to 0.59 mm. For the dynamic layer height control, R_t changes negligibly (from 76.00 to 65.63 μm) and t decreases from 0.68 to 0.59 mm with increasing α, which validates the effectiveness of the dynamic layer height control strategy to make smooth surfaces.

For complex 3D structure printing, slicing using dynamic layer height control enhances the uniform distribution of surface roughness. An *L*-shaped tube is printed via constant layer height control and dynamic layer height control, respectively. The slicing strategy and generated printing trajectories are detailed in *SI Appendix*, Fig. S4. Four representative positions are selected to measure localized surface roughness, as shown in the *Inset* of Fig. 3*D*. Dynamically slicing the *L*-shaped tube not only controls the surface roughness at a relatively low level (76.27 μm) but also ensures the smooth surfaces in both the vertical tube section (measured position 1) and different cross-sections in the horizontal tube section (measured positions 2 to 4). Conversely, constantly slicing the *L*-shaped tube can only achieve low surface roughness at given locations (measured positions 1 and 3). On the top and bottom of the horizontal tube section, the surface roughness exceeds 300.00 μm and filaments even detach from each other (*Inset* of Fig. 3*D*).

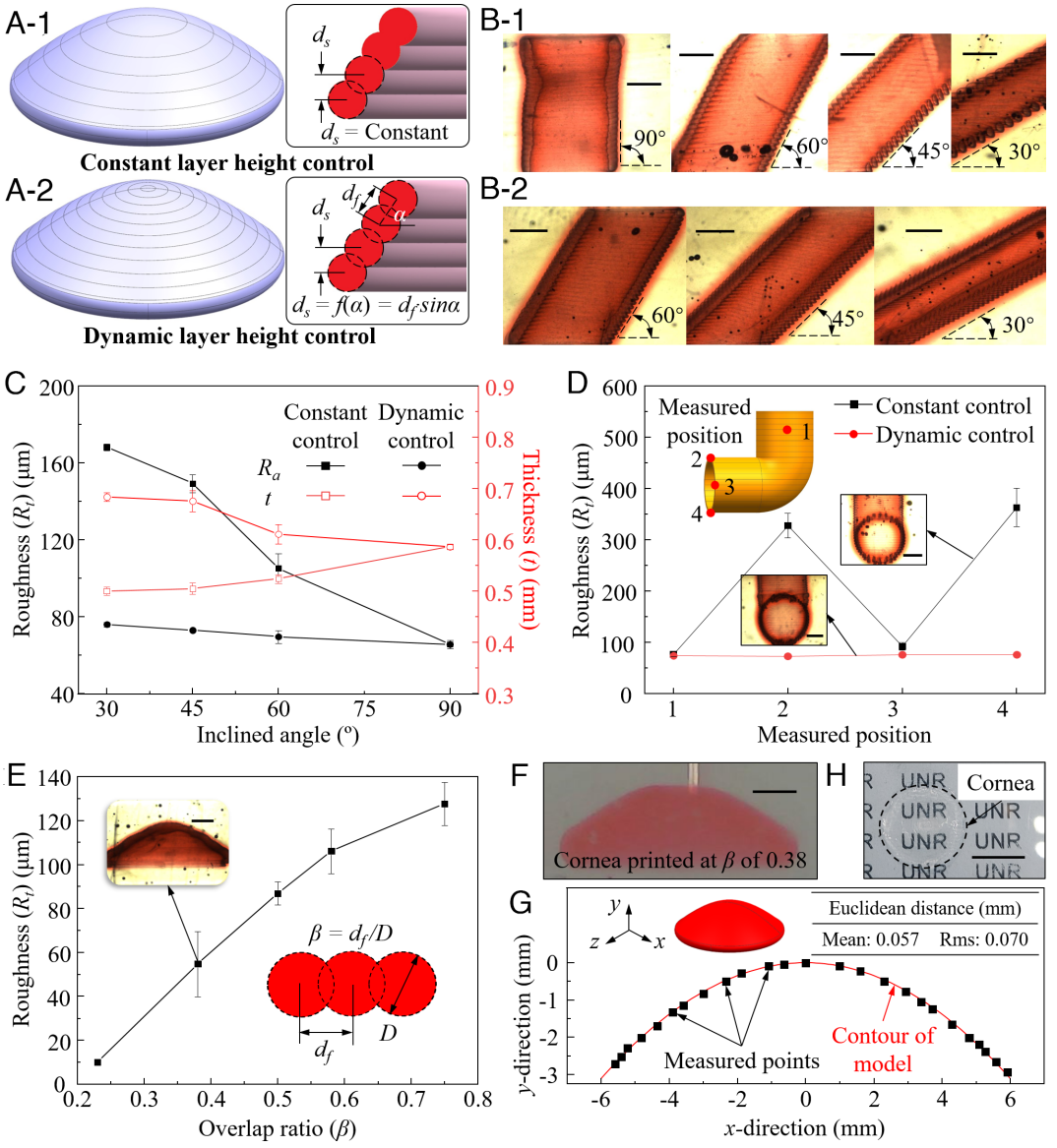

Fig. 3. 3D printing of the high-precision human cornea by using MSEP and dynamic layer height control strategy. (*A*-1) Constant layer height control strategy in current 3D printing approaches. (*A*-2) Proposed dynamic layer height control strategy. Inclined tubes printed by (*B*-1) constant layer height control and (*B*-2) dynamic layer height control. (Scale bars, 2.0 mm.) (*C*) Roughness and wall thickness of inclined tubes printed by different layer height control strategies. (*D*) Distribution of roughness on *L*-shaped tubular structures printed by different layer height control strategies. (Scale bars, 2.0 mm.) (*E*) Effects of overlap ratio on surface roughness of cornea structures printed by dynamic layer height control. (Scale bar, 1.0 mm.) (*F*) MSEP of the engineered cornea with a surface roughness of 54.70 μm. (Scale bar, 2.0 mm.) (*G*) Evaluation of shape accuracy of the printed cornea. (*H*) Engineered cornea from GelMA with good transparency. (Scale bar, 10.0 mm.) The quantitative values in *C*–*E* are reported as means ± SD with n = 3 samples per group.

In addition to layer height control, surface roughness is also affected by overlap ratio (β), which is defined as the ratio of d_f to filament diameter (D), as illustrated in the *Inset* of Fig. 3*E*. When β increases from 0.25 to 1.25, R_t increases greatly from 31.47 to 167.67 μm (*SI Appendix*, Fig. S5A), while the thickness of the printed sample decreases from 1.79 to 0.41 mm (*SI Appendix*, Fig. S5B). The coupling effects of layer height control and β are investigated by printing cornea structures with different β values and variable d_s. The surface roughness of each cornea is measured and summarized in Fig. 3*E*. It is observed that R_t can be tuned in a large range from 10.07 to 127.60 μm. Thus, an engineered cornea is printed at the β of 0.38, which has a surface roughness of 54.70 μm, as shown in Fig. 3*F* and Movie S1. In addition, the effect of this new layer height control strategy on the overall shape accuracy of the printed cornea is illustrated in Fig. 3*G*. Twenty-five points on the cornea profile are picked and the Euclidean distance from each point to the model profile is calculated. The mean distance is only 0.057 mm, validating that the shape accuracy is also guaranteed when using the dynamic layer height control. Finally, based on the obtained knowledge, an engineered cornea from GelMA is printed, which presents good transparency, as demonstrated in Fig. 3*H*. In this work, R_t is directly measured via software and used to quantify the surface quality, which is statistically three to nine times higher than arithmetical mean roughness (R_a). After conversion, the printed cornea has the R_a value between 6.08 to 18.23 μm. Therefore, as compared to other extrusion printed structures that have a common R_a range of over 100.00 μm (65), the proposed dynamic layer height control strategy can significantly improve the surface morphology. It is noted that the R_a of the human cornea falls in the range of 0.23 to 0.36 μm (22). Future work will focus on decreasing filament diameter, another key factor to affect the resolution of printed products, which may further expand the functional feature size scope of MSEP to the order of submicrons.

3D Printing of Mesoscale Eyeballs and Aortic Valves. Eyeball is a sophisticated organ with a multilayered, chambered architecture. It is challenging to print such a structure using conventional embedded ink writing approaches because residual support bath materials encapsulated in the chamber are difficult to remove. In this study, we will print human eyeball equivalents using MSEP to demonstrate the feasibility of this printing approach. First, filament size control in the thermosensitive yield-stress support bath is investigated. The effects of path speed on filament diameter are illustrated in Fig. 4*A*. With the increase of path speed, filament diameter decreases, which is consistent with the reported results (3, 18, 37). Based on the relationship, path speed can be selected to form desired filaments to construct eyeballs and other tissue and organ equivalents. In addition, the roles of nozzle diameter and dispensing pressure in filament formation are demonstrated in *SI Appendix*, Fig. S6 *A* and *B*, respectively. Filament diameter increases with the increase of either nozzle diameter or dispensing pressure. When printing in a yield-stress support bath, each filament remains liquid before undergoing cross-linking. The diffusion of ink material from the filament into the surrounding support bath may cause filament enlargement in a long time. Thus, the filament diameter change over time is characterized, as shown in Fig. 4*B*. Immediately after printing, the filament has a diameter of 414.71 μm. After submerging in the support bath for 15 h, the filament diameter increases to 448.17 μm with a swelling ratio of only 8.08%. This is because the diffusion of hydrogel molecules is not only dependent on the concentration difference (66) but also affected by the microstructure of surrounding media. Generally, a densified microstructure can hinder the passage of large hydrogel molecules, weakening the diffusion process (67). In this work, the dual microstructure formed within the support bath inhibits the diffusion of NaAlg and PEGDA molecules into the bath, resulting in the formation of filaments with excellent stability.

After understanding filament formation and stability, a homogenous human eyeball equivalent is printed in the support bath, as

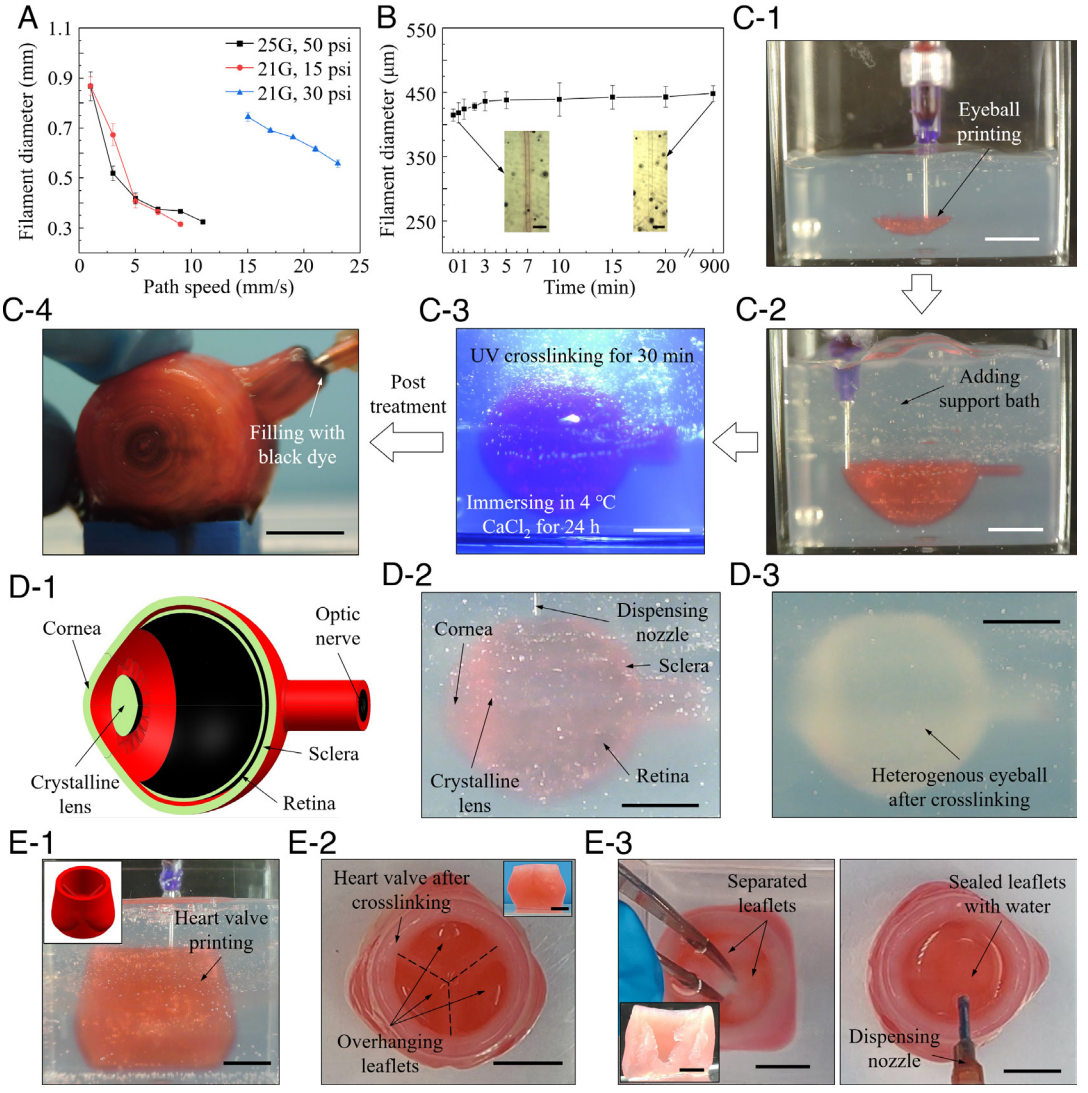

Fig. 4. 3D printing of mesoscale eyeballs with optical nerve structures and aortic heart valve with overhanging leaflets. (*A*) Filament diameter as a function of path speed. (*B*) Filament diameter change over time in the thermosensitive yield-stress support bath. (Scale bars, 1.00 mm.) (*C*) Homogenous eyeball printing: (*C*-1) printing the bottom section in the support bath at room temperature; (*C*-2) perfusing additional support bath material at 4 °C into the container; (*C*-3) UV cross-linking of PEGDA component and ionic cross-linking of NaAlg component in the printed eyeball equivalent; and (*C*-4) post-treatment to the eyeball equivalent. (*D*) Heterogenous eyeball printing: (*D*-1) anatomical architecture of human eyeball; (*D*-2) eyeball reconstruction using a dual extruder 3D printer; and (*D*-3) heterogenous eyeball after cross-linking. (*E*) Aortic heart valve with overhanging leaflets: (*E*-1) heart valve printing in the support bath (*Inset*: design of the human heart valve); (*E*-2) cross-linked heart valve releasing from the support bath (*Inset*: front view of the valve); and (*E*-3) heart valve with three separated leaflets [*Inset*: cross-section of the valve (scale bar, 5.0 mm)] and sealed leaflets with water. (Scale bars, 10.0 mm.) The quantitative values in *A* and *B* are reported as means ± SD with $n = 3$ samples per group.

shown in Movie S2. The eyeball model is divided into two sections. The bottom section is printed first at room temperature, as illustrated in Fig. 4 *C*-1. Since this temperature is higher than T_{cm}, the support bath presents a yield-stress property. The movement of the dispensing nozzle disturbs the interactive dual microstructure within the nanocomposite, leading to the localized liquefication of the bath material and allowing for the free deposition of bioinks. When the nozzle moves away, the reduction of shear stress results in the recovery of the dual microstructure. Thus, the support bath switches to the solid-like state to stably hold the printed eyeball section in situ. After completing the bottom section, additional support bath material at 4 °C is perfused into the container. At such a low temperature, the nanocomposite shows a low viscosity (Fig. 2*B*) and good flowability so that the newly added nanocomposite can rapidly and uniformly fill the container, as shown in Fig. 4 *C*-2. Once the top section is completed, ionic and UV cross-linking are applied by immersing the support bath in a calcium chloride ($CaCl_2$) bath at 4 °C while being exposed to UV radiation (Fig. 4 *C*-3). Because the ambient temperature is below T_{cm}, the nanocomposite switches to the sol state, and calcium ions diffuse through the liquefied support bath which causes the cross-linking of the NaAlg component in the printed eyeball. During UV radiation, PEGDA is photocross-linked. The formed interpenetrating polymer networks between NaAlg and PEGDA further enhance the mechanical stiffness of the eyeball, making it easy to remove from the support bath. Post-treatment is finally performed to the eyeball equivalent, as recorded in Movie S3, in which the eyeball construct is first placed in the refrigerator to liquefy the residual support bath material encapsulated in the chamber. Then, a nozzle is inserted into the chamber to exhaust the support bath material. Finally, deionized (DI) water with black dye is injected to validate that the chamber is hollow, as shown in Fig. 4 *C*-4. The key dimensions (*SI Appendix*, Fig. S7) are measured. Particularly, the optic nerve has a designed diameter of 3.80 mm and a measured diameter of 3.86 mm. The relative error is only 1.58%, which demonstrates the high accuracy of the proposed MSEP approach. Two more eyeball equivalents are also printed and their key dimensions are measured, as shown in *SI Appendix*, Table S3, which present good consistency, validating the outstanding robustness of the MSEP approach.

A human eyeball is composed of multiple sections (cornea, crystalline lens, sclera, retina, optic nerve, etc.), as shown in Fig. 4 *D*-1. In this work, a dual extruder 3D printer is used to print a heterogenous eyeball equivalent from two bioinks: GelMA and NaAlg/PEGDA. The fabrication protocol is similar to that for reconstructing the homogenous eyeball architecture. Specifically, the GelMA bioink with a black dye is applied to print the retina, crystalline lens, and optic nerve, while the NaAlg/PEGDA bioink with a red dye is used to construct other sections, as shown in Fig. 4 *D*-2. The fabrication process is recorded in Movie S4. Because the sections from both bioinks remain liquid during printing, they can fuse well with each other to enhance the mechanical stiffness at the interfaces after UV cross-linking (Fig. 4 *D*-3). As shown in *SI Appendix*, Fig. S8, the tensile specimens made from dissimilar bioinks fracture at the end with lower elastic modulus (i.e., the half made from GelMA), instead of at the interface, which shows the feasibility of MSEP to print complex human organs from multiple build materials with good interfacial bonding.

Another representative human tissue with mesoscale functional feature sizes is the aortic heart valve, which is composed of a sinus wall and three overhanging leaflets, as shown in the *Inset* of Fig. 4 *E*-1. In conventional extrusion-based 3D bioprinting approaches (e.g., direct ink writing), temporary support scaffolds need to be printed to hold the overhanging leaflets before cross-linking, which not only makes the post-treatments complicated but may also cause damage to the printed heart valve (57, 68–70). Such architecture is easy to achieve via MSEP because the yield-stress bath can support uncured heart valve construct in situ. The result is illustrated in Fig. 4 *E*-1 as well as Movie S5. After cross-linking via UV radiation and $CaCl_2$, three leaflets can be distinguished from each other (Fig. 4 *E*-2). The key dimensions of three heart valve equivalents are measured in *SI Appendix*, Table S4 to validate the repeatability of the MSEP approach. Specifically, the thickness of each leaflet is designed as 1.00 mm, and the printed valves have leaflet thicknesses of around 1.04, 0.93, and 1.05 mm, respectively. The relative errors are only 4.0, 7.0, and 5.0%, proving the high accuracy of the printed heart valve equivalents. The cross-section of the heart valve is shown in the *Inset* of Fig. 4 *E*-3, from which the sinus wall and overhanging leaflets can be observed. The diastole and systole status of the heart valve equivalent are demonstrated in Fig. 4 *E*-3. Three leaflets can separate from each other under unidirectional force and seal tightly when the force is removed (Movie S6). DI water is dipped into the heart valve at the systole status (*Right* in Fig. 4 *E*-3) and no leakage is observed. Therefore, the printed valve has the potential to be used as a prosthesis for heart valve replacement in the future.

3D Printing of Full-Scale Human Heart Construct. In this work, a full-scale human heart is printed to prove that MSEP is capable of reconstructing tissues and organs with large sizes. Cross-linking depth is investigated to explore whether the engineered human heart can be fully cured under UV radiation. The effects of exposure time and UV intensity on the cross-linking depth are characterized as shown in Fig. 5 *A* and *B*, respectively. It is observed that cross-linking depth increases greatly from 0 to 27.31 mm after 15-min exposure to UV radiation. From 15 to 30 min, the cross-linking depth increases slightly from 27.31 to 30.47 mm. As a result, the maximum cross-linking depth for the NaAlg/PEGDA bioink is around 30.00 mm. Because the designed human heart has the overall dimensions of 81.31 × 64.14 × 53.59 mm^3, bidirectional UV radiation can ensure the complete cross-linking of a printed heart. In addition, the cross-linking depth increases with increasing UV intensity. The theoretical cross-linking depth (C_d) in photopolymerization can be qualitatively analyzed using Eq. **6** (71):

$$C_d = D_p \ln\left(E_{max} / E_c\right), \quad [6]$$

where D_p is the penetration depth of UV light into a photocurable material until a reduction in irradiance of $1/e$ is reached, E_{max} is the maximum exposure of UV light, and E_c is the critical exposure at which UV cross-linking starts to occur. In this work, E_{max} is equivalent to UV intensity. Therefore, when two material-related parameters (D_p and E_c) are constant, the rise in UV intensity leads to the increase in cross-linking depth.

Since ionic cross-linking is needed to solidify the NaAlg component, the penetration depth is measured experimentally, in which calcium ions can only diffuse unidirectionally into the bioink encapsulated in a tube (*Inset* of Fig. 5*C*). As shown in Fig. 5*C*, the penetration depth increases with submerging time. In the cross-linking step during heart fabrication, the entire support bath is submerged in the $CaCl_2$ bath, which results in the multidirectional diffusion of calcium ions. Therefore, the exposure time and submerging time are determined to be 30 min and 48 h, respectively, based on the heart geometries and measured data.

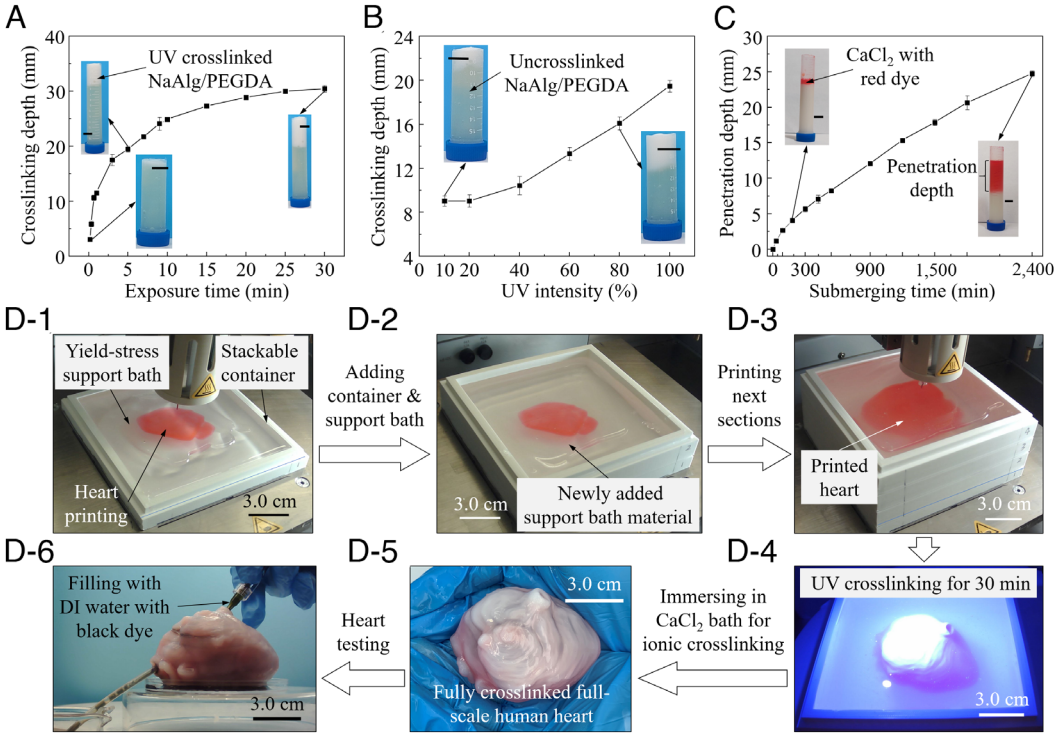

Fig. 5. 3D printing of full-scale human heart equivalent via MSEP. Cross-linking depth as a function of (*A*) exposure time and (*B*) UV intensity during photocross-linking. (*C*) Penetration depth as a function of submerging time during ionic cross-linking. (*D*) Full-scale human heart printing: (*D*-1) first section printing at room temperature using a short dispensing nozzle; (*D*-2) adding the support bath material at 4 °C; (*D*-3) printed full-scale human heart after repeating the bioink printing-support bath adding cycle for four times; (*D*-4) UV cross-linking of the printed heart for 30 min; (*D*-5) engineered human heart equivalent after ionic cross-linking; and (*D*-6) heart chamber testing by perfusing DI water with black dye. (Scale bars, 10.0 mm.) The quantitative values in *A*–*C* are reported as means ± SD with $n = 3$ samples per group.

The full-scale human heart is divided into four sections and sequentially printed within the thermosensitive yield-stress support bath using a short dispensing nozzle with a length of 12.70 mm (Movie S7). A stackable container consisting of four pieces is designed for this purpose. After the first section of the heart is printed at room temperature (Fig. 5 *D*-1), the second piece of the container is added, and then the nanocomposite at 4 °C is perfused into the container, as shown in Fig. 5 *D*-2. When the temperature of the newly added nanocomposite reaches the working temperature, the second section of the heart can be printed. By repeating this bioink printing-support bath adding cycle four times, the full-scale human heart equivalent is successfully printed (Fig. 5 *D*-3). The cross-linking step and post-treatments can be seen in Movie S8. Particularly, after cross-linking under UV radiation for 30 min (Fig. 5 *D*-4), the printed heart with the surrounding support bath material is immersed in the $CaCl_2$ bath at 4 °C for ionic cross-linking. The achieved heart is illustrated in Fig. 5 *D*-5, and its key dimensions (*SI Appendix*, Fig. S10) are measured, as shown in *SI Appendix*, Table S5. After removing the residual support bath material from the heart chambers at 4 °C, DI water with black dye is injected into the heart from the inferior vena cava, which can flow out of the heart from the aorta, as shown in Fig. 5 *D*-6 and Movie S9.

From the processing perspective, cell damage in embedded ink writing is mainly affected by shear stress τ_N and shearing time t_N of cells exposed to shear stress, which cause cell deformation when passing through a nozzle. When the deformation exceeds a threshold value (72), damages to the bilipid layer membrane or cortical cytoskeleton eventually lead to irreversible cell damage, resulting in dead cells. The total amount of damaged cells during extrusion (CD_{total}) can be described by: $CD_{total} = CD_{unit} \cdot L_N = d_c \int_0^{R_N} 2\pi r I_c(\tau_N, t_N) dr \cdot L_N$, where CD_{unit} is the number of damaged cells in a unit length, L_N is the nozzle length, d_c is the cell density, R_N is the nozzle radius, r is the radial direction of the nozzle, and I_c is the cell damage law: $I_c(\tau_N, t_N) = \int_{t_N}\int_{\tau_N} f(\tau_N, t_N)\, d_{\tau_N} d_{t_N}$, where $f(\tau_N, t_N)$ is the probability density function. Particularly, t_N and τ_N can be described by $t_N = L_N / v_N$ and $\tau_N = P \cdot r / 2L_N = v_N \eta_0^{ink} r / (R_N^2 - r^2)$, respectively (73), where v_N is the velocity distribution in the nozzle $v_N = P \cdot (R_N^2 - r^2) / 2\eta_0^{ink} L_N$ (74), P is the dispensing pressure, and η_0^{ink} is the cellular ink's zero-shear-rate viscosity. Thus, the increase of L_N directly leads to the increase of CD_{total} and t_N. Moreover, because functional tissue/organ construction needs high density of functional cells for proliferation and differentiation, η_0^{ink} is usually high which requires higher P to achieve a constant v_N compared to that of acellular inks, especially when L_N is large. Therefore, τ_N also increases that results in the further increment of CD_{total}. In the proposed MSEP, a short dispensing nozzle is applied to print full-scale human tissue and organ equivalents in a section-by-section manner, which can effectively minimize cell damage during printing and achieve a high cell viability. From the material perspective, all materials used in this work, including the GelMA bioink and the nanoclay-Pluronic F127 nanocomposite, exhibit excellent biocompatibility (75–77), making the MSEP strategy promising for cell printing applications.

Conclusions

In this work, we develop an MSEP strategy to print human tissue and organ equivalents with functional feature sizes on the orders from

microns to tens of centimeters. A thermosensitive yield-stress support bath is developed to facilitate MSEP. The temperature-induced microstructure evolution enables the support bath material to possess desired rheological behaviors for both 3D structure printing and support bath adding purposes. Thus, it is feasible to use a short dispensing nozzle to print full-scale human tissue and organ equivalents with larger overall sizes. The maximum size may only be constrained by the travel range of used 3D printer. Herein, a dynamic layer height control strategy is implemented, which not only overcomes the layered morphology in existing extrusion-based 3D bioprinting methods but also allows smooth surfaces to be uniformly distributed in complex 3D structures. Using this strategy, a smooth-surfaced cornea with micron-level surface roughness has been printed. The support bath material can be liquefied at lower temperatures, making it easy to remove after printing. Using this merit, both homogenous and heterogeneous human eyeballs and aortic heart valves are reconstructed. Finally, a full-scale human heart on the order of tens of centimeters is fabricated by adding the support bath material on demand during printing. The proposed MSEP presents a broader printing capability space. Particularly, using a short dispensing nozzle to print large structures can effectively minimize cell damage during extrusion, which makes the fabrication of implantable human tissues and organs technically feasible. In addition, the MSEP approach can also be applied in different fields, such as wearable sensors and soft robotics, to deposit functional inks with high viscosity into complex geometries with high resolution. Although MSEP presents various advantages, there are still some limitations. On one hand, when adding support bath materials during printing, users have to wait for a specific duration to allow the support bath temperature increase to working temperature, which lowers the fabrication efficiency. 3D printers specifically designed for MSEP is a potential solution which can rapidly and accurately control the environment temperature for enhancing the fabrication efficiency. On the other hand, the support bath material in the proposed MSEP is thermosensitive, thereby limiting the printing of some thermosensitive biomaterials, such as collagen. To tackle this challenge, yield-stress fluids that are sensitive to other external stimuli, such as photo radiation, will be developed.

Since the focus of this study is placed on the development of MSEP and demonstration of its printing capability, cell-related investigations have not been systematically performed yet. However, the utilization of a short dispensing nozzle in the work can effectively reduce shear stress during cell-laden bioink extrusion, allowing the proposed MSEP to be expandable for printing scaled-up constructs with living cells. Therefore, our future work will include: 1) Testing cell behaviors in MSEP. Living cells, like valvular endothelial cells (VECs) and/or valvular interstitial cells (VICs), will be extruded through short dispensing nozzles to explore the interrelationships between nozzle geometries, cell density, and behaviors; 2) Printing 3D constructs with cellular heterogeneity. Heterogenous eyeballs have been printed in this work. We will reconstruct aortic heart valves with both VECs and VICs to further validate the heterogeneous capability of MSEP; and 3) Accelerating printing process. Total printing time also plays an important role when fabricating cellular constructs. The developed thermosensitive yield-stress support bath functions well at a path speed of around 20.0 mm/s. Higher speeds (from 20.0 to 100.0 mm/s) will be tested in the future for realizing the high-speed 3D bioprinting of human tissues and organs.

Materials and Methods

Materials. In this work, the nanoclay-Pluronic F127 nanocomposite was prepared as the thermosensitive yield-stress support bath. The NaAlg/PEGDA mixture was used as the bioink material for printing human tissue and organ equivalents. The GelMA bioink was prepared for printing the transparent cornea and given components of the heterogenous human eyeball. Calcium chloride was utilized to ionically cross-link the NaAlg component of the bioink. The detailed steps for material preparation were included in Supporting Information.

Material Characterization. The rheological properties of the thermosensitive yield-stress support bath as well as the NaAlg/PEGDA bioink were measured by the rheometer. The microstructures of the support bath material were characterized by the SANS diffractometer and TEM, respectively, at the Oak Ridge National Laboratory. UV transparency of the support bath was measured using the UV/Vis spectrophotometer. Mechanical properties of the bioinks were characterized by the ADMET mechanical tester. The bioink degradation was characterized by monitoring the mass loss ratio in 14 d. Both UV cross-linking depth and ionic cross-linking depth were characterized by observing the phase/color change of the NaAlg/PEGDA ink within a homemade tubular tool. The detailed steps for material characterization were included in Supporting Information.

3D Structure Printing and Characterization. The EFL 3D bioprinter was used to print tubular structures, *L*-shaped tubes, quarter-ring sheets, and flat sheets within the support bath to investigate the effects of two layer height control strategies and overlap ratio on the surface roughness and thickness. The high-precision measurement system was applied to measure the key geometrical parameters. Cornea constructs from the NaAlg/PEGDA bioink and the GelMA bioink were printed by the EFL 3D bioprinter, respectively, to study the surface roughness, overall shape accuracy, and transparency. The same 3D bioprinter was also applied to print filaments within the thermosensitive yield-stress support bath to investigate the effects of printing parameters on filament formation. The EnvisionTEC 3D bioplotter was utilized to print the engineered eyeballs, aortic heart valves, and full-scale human hearts at room temperature. The detailed steps for 3D structure printing, post-treatments, and print characterization were all included in Supporting Information.

Data, Materials, and Software Availability. All study data are included in the article and/or supporting information. Additional data is available from the corresponding author (yifeij@unr.edu) upon reasonable request.

ACKNOWLEDGMENTS. C.Z. and W.H. contributed equally to this work. The TEM research was conducted as part of a user project at the Center for Nanophase Materials Sciences, which is a US Department of Energy (DOE), Office of Science User Facility at Oak Ridge National Laboratory. This research also used resources at the Spallation Neutron Source, a DOE Office of Science User Facility operated by the Oak Ridge National Laboratory. L.R. would like to acknowledge the support of the NSF Graduate Research Fellowship Program through NSHE subaward number: AWD0002282-1937966. R.C. would like to acknowledge the support of the NSF Graduate Research Fellowship Program through NSHE subaward number: AWD01-00002282. L.W. acknowledges the support of the NIH (COBRE P20GM130459) and the American Heart Association (Career Development Award 942098). D.Z. acknowledges the support of the National Key R&D Program of China (2018YFA0703000) and the National Natural Science Foundation of China (52175289). G.C. acknowledges the support of the Liaoning Provincial Natural Science Foundation of China (2022-YGJC-27). Y.J. acknowledges the support of the NSF (OIA-2229004).

Author affiliations: [a]Department of Mechanical Engineering, University of Nevada, Reno, NV 89557; [b]State Key Laboratory of High-Performance Precision Manufacturing, School of Mechanical Engineering, Dalian University of Technology, Dalian 116024, China; [c]Department of Industrial and Manufacturing Systems Engineering, Iowa State University, Ames, IA 50011; [d]Department of Pharmacology, Center for Molecular and Cellular Signaling in the Cardiovascular System, School of Medicine, University of Nevada, Reno, NV 89557; [e]Neutron Scattering Division, Oak Ridge National Laboratory, Oak Ridge, TN 37831-6475; [f]Center for Nanophase Materials Sciences, Oak Ridge National Laboratory, Oak Ridge, TN 37830; [g]Department of Chemistry, University of Nevada, Reno, NV 89557; [h]Three-Dimensional Advanced Visualization Laboratory, Department of Pediatric Radiology, Children's Hospital & Medical Center, Omaha, NE 68114; [i]School of Naval Architecture and Ocean Engineering, Huazhong University of Science and Technology, Wuhan 430074, China; [j]Mary & Dick Holland Regenerative Medicine Program, Division of Cardiovascular Medicine, Department of Internal Medicine, University of Nebraska Medical Center, Omaha, NE 68198; and [k]Department of Ophthalmology, Shengjing Hospital of China Medical University, Shenyang 110004, China

1. E. M. Shen, K. E. Mccloskey, Affordable, high-resolution bioprinting with embedded concentration gradients. *Bioprinting* **21**, e00113 (2021).
2. C. Caneparo, D. Brownell, S. Chabaud, S. Chabaud, S. Bolduc, Genitourinary tissue engineering: Reconstruction and research models. *Bioengineering* **8**, 99 (2021).
3. Y. Jin, W. Chai, Y. Huang, Printability study of hydrogel solution extrusion in nanoclay yield-stress bath during printing-then-gelation biofabrication. *Mater. Sci. Eng. C Mater. Biol. Appl.* **80**, 313–325 (2017).
4. S. Lee *et al.*, Human-recombinant-elastin-based bioinks for 3D bioprinting of vascularized soft tissues. *Adv. Mater.* **32**, e2003915 (2020).
5. A. Tejo-Otero, I. Buj-Corral, F. Fenollosa-Artés, 3D printing in medicine for preoperative surgical planning: A review. *Ann. Biomed. Eng.* **48**, 536–555 (2020).
6. D. Shopova *et al.*, (Bio)printing in personalized medicine–Opportunities and potential benefits. *Bioengineering* **10**, 287 (2023).
7. G. Bao *et al.*, Triggered micropore-forming bioprinting of porous viscoelastic hydrogels. *Mater. Horiz.* **7**, 2336–2347 (2020).
8. H. Savoji *et al.*, 3D printing of vascular tubes using bioelastomer prepolymers by freeform reversible embedding. *ACS Biomater. Sci. Eng.* **6**, 1333–1343 (2020).
9. J. Huang *et al.*, 3D bioprinting of hydrogels for cartilage tissue engineering. *Gels* **7**, 144 (2021).
10. N. Noor *et al.*, 3D printing of personalized thick and perfusable cardiac patches and hearts. *Adv. Sci.* **3**, 1900344 (2019).
11. M. E. Scarritt, N. C. Pashos, B. A. Bunnell, A review of cellularization strategies for tissue engineering of whole organs. *Front. Bioeng. Biotechnol.* **3**, 43 (2015).
12. H. Gudapati, M. Dey, I. Ozbolat, A comprehensive review on droplet-based bioprinting: Past, present and future. *Biomaterials* **102**, 20–42 (2016).
13. D. Zhou *et al.*, Bioinks for jet-based bioprinting. *Bioprinting* **16**, e00060 (2019).
14. Y. Jin *et al.*, Nanoclay suspension-enabled extrusion bioprinting of three-dimensional soft structures. *J. Manuf. Sci. Eng.* **143**, 121004 (2021).
15. Y. Jin, A. Compaan, T. Bhattacharjee, Y. Huang, Granular gel support-enabled extrusion of three-dimensional alginate and cellular structures. *Biofabrication* **8**, 025016 (2016).
16. K. Elkhoury, J. Zuazola, S. Vijayavenkataraman, Bioprinting the future using light: A review on photocrosslinking reactions, photoreactive groups, and photoinitiators. *SLAS Technol.* **28**, 142–151 (2023).
17. P. Wang *et al.*, Extrusion-based 3D co-printing: Printing material design and novel workflow for fabricating patterned heterogeneous tissue structures. *Mater. Des.* **227**, 111737 (2023).
18. M. Rocca, A. Fragasso, W. Liu, M. A. Heinrich, Y. S. Zhang, Embedded multimaterial extrusion bioprinting. *SLAS Technol.* **23**, 154–163 (2018).
19. J. J. Senior, M. E. Cooke, L. M. Grover, A. M. Smith, Fabrication of complex hydrogel structures using suspended layer additive manufacturing (SLAM). *Adv. Funct. Mater.* **29**, 1904845 (2019).
20. S. Hassan *et al.*, Tunable and compartmentalized multimaterial bioprinting for complex living tissue constructs. *ACS Appl. Mater. Interfaces* **14**, 51602–51618 (2022).
21. S. J. Mccafferty, J. T. Schwiegerling, E. T. Enikov, Corneal surface asphericity, roughness, and transverse contraction after uniform scanning excimer laser ablation. *Invest. Ophthalmol. Vis. Sci.* **53**, 1296–1305 (2012).
22. J. Gros-Otero *et al.*, Corneal stromal roughness after VisuMax and Intralase femtosecond laser photodisruption: An atomic force microscopy study. *PLoS ONE* **16**, e0252449 (2021).
23. D. H. Kim, J. S. Jun, R. Kim, Measurement of the optic nerve sheath diameter with magnetic resonance imaging and its association with eyeball diameter in healthy adults. *J. Clin. Neurol.* **14**, 345–350 (2018).
24. M. C. Sapp, H. J. Fares, A. C. Estrada, K. J. Grande-Allen, Multilayer three-dimensional filter paper constructs for the culture and analysis of aortic valvular interstitial cells. *Acta. Biomater.* **13**, 199–206 (2015).
25. S. Mohammadi *et al.*, Study of the normal heart size in Northwest part of Iranian population: A cadaveric study. *J. Cardiovasc. Torac. Res.* **8**, 119–125 (2016).
26. T. J. Hinton *et al.*, Three-dimensional printing of complex biological structures by freeform reversible embedding of suspended hydrogels. *Sci. Adv.* **1**, e1500758 (2015).
27. E. Mirdamadi, J. W. Tashman, D. J. Shiwarski, R. N. Palchesko, A. W. Feinberg, FRESH 3D bioprinting a full-size model of the human heart. *ACS Biomater. Sci. Eng.* **6**, 6453–6459 (2020).
28. A. Lee *et al.*, 3D bioprinting of collagen to rebuild components of the human heart. *Science* **365**, 482–487 (2019).
29. O. Jeon, Y. B. Lee, T. J. Hinton, A. W. Feinberg, E. Alsberg, Cryopreserved cell-laden alginate microgel bioink for 3D bioprinting of living tissues. *Mater. Today Chem.* **12**, 61–70 (2019).
30. A. R. Spencer *et al.*, Bioprinting of a cell-laden conductive hydrogel composite. *ACS Appl. Mater. Interfaces* **11**, 30518–30533 (2019).
31. S. Abdollahi, A. Davis, J. H. Miller, A. W. Feinberg, Expert-guided optimization for 3D printing of soft and liquid materials. *PLoS ONE* **13**, e0194890 (2018).
32. T. Bhattacharjee *et al.*, Writing in the granular gel medium. *Sci. Adv.* **1**, e1500655 (2015).
33. T. J. Hinton, A. Hudson, K. Pusch, A. Lee, A. W. Feinberg, 3D printing PDMS elastomer in a hydrophilic support bath via freeform reversible embedding. *ACS Biomater. Sci. Eng.* **2**, 1781–1786 (2016).
34. L. Ning *et al.*, Embedded 3D bioprinting of gelatin methacryloyl-based constructs with highly tunable structural fidelity. *ACS Appl. Mater. Interfaces* **12**, 44563–44577 (2020).
35. K. Zhou, M. Feng, H. Mao, Z. Gu, Photoclick polysaccharide-based bioinks with an extended biofabrication window for 3D embedded bioprinting. *Biomater. Sci.* **10**, 4479–4491 (2022).
36. Y. Jin, A. Compaan, W. Chai, Y. Huang, Functional nanoclay suspension for printing-then-solidification of liquid materials. *ACS Appl. Mater. Interfaces* **9**, 20057–20066 (2017).
37. B. B. Mendes *et al.*, Human platelet lysate-based nanocomposite bioink for bioprinting hierarchical fibrillar structures. *Biofabrication* **12**, 015012 (2019).
38. M. A. Skylar-Scott *et al.*, Biomanufacturing of organ-specific tissues with high cellular density and embedded vascular channels. *Sci. Adv.* **5**, eaaw2459 (2019).
39. C. S. O'bryan *et al.*, Self-assembled micro-organogels for 3D printing silicone structures. *Sci. Adv.* **3**, e1602800 (2017).
40. Y. Wu, A. Wenger, H. Golzar, X. Tang, 3D bioprinting of bicellular liver lobule-mimetic structures via microextrusion of cellulose nanocrystal-incorporated shear-thinning bioink. *Sci. Rep.* **10**, 20648 (2020).
41. O. Jeon *et al.*, Individual cell-only bioink and photocurable supporting medium for 3D printing and generation of engineered tissues with complex geometries. *Mater. Horiz.* **6**, 1625–1631 (2019).
42. A. M. Compaan, K. Song, W. Chai, Y. Huang, Cross-linkable microgel composite matrix bath for embedded bioprinting of perfusable tissue constructs and sculpting of solid objects. *ACS Appl. Mater. Interfaces* **12**, 7855–7868 (2020).
43. Y. J. Choi *et al.*, A 3D cell printed muscle construct with tissue-derived bioink for the treatment of volumetric muscle loss. *Biomaterials* **206**, 160–169 (2019).
44. F. Afghah, M. Altunbek, C. Dikyol, B. Koc, Preparation and characterization of nanoclay-hydrogel composite support-bath for bioprinting of complex structures. *Sci. Rep.* **10**, 5257 (2020).
45. W. Hua *et al.*, Three-dimensional printing in stimuli-responsive yield-stress fluid with an interactive dual microstructure. *ACS Appl. Mater. Interfaces* **14**, 39420–39431 (2022).
46. G. Wanka, H. Hoffmann, W. Ulbricht, Phase diagrams and aggregation behavior of poly(oxyethylene)-poly(oxypropylene)-poly(oxyethylene) triblock copolymers in aqueous solutions. *Macromolecules* **27**, 4145–4159 (1994).
47. A. A. Barba *et al.*, Investigation of Pluronic© F127–Water solutions phase transitions by DSC and dielectric spectroscopy. *J. Appl. Polym. Sci.* **114**, 688–695 (2009).
48. A. Nelson, T. Cosgrove, Small-angle neutron scattering study of adsorbed pluronic tri-block copolymers on laponite. *Langmuir* **21**, 9176–9182 (2005).
49. T. D. C. Chaparro *et al.*, Interaction of cationic, anionic, and nonionic macroraft homo- and copolymers with laponite clay. *Langmuir* **35**, 11512–11523 (2019).
50. S. Park *et al.*, Silicones for stretchable and durable soft devices: Beyond Sylgard-184. *ACS Appl. Mater. Interfaces* **10**, 11261–11268 (2018).
51. T. Kosta, T. R. Krawietz, J. O. Mares Jr., "Sylgard 184 mixture and natural aging study via quasi-static compressive modulus" in *Proceedings of the Conference of the American Physical Society Topical Group on Shock Compression of Condensed Matter*, J. M. D. Lane, T. C. Germann, M. R. Armstrong, R. Wixom, D. Damm, J. Zaug, Eds. (AIP Publishing, Portland, OR, 2020), pp. 040007-1–040007-5.
52. A. Nelson, T. Cosgrove, A small-angle neutron scattering study of adsorbed poly(ethylene oxide) on laponite. *Langmuir* **20**, 2298–2304 (2004).
53. H. Matsuoka, H. Tanaka, T. Hashimoto, N. Ise, Elastic scattering from cubic lattice systems with paracrystalline distortion. *Phys. Rev. B, Condens. Matter.* **36**, 1754–1765 (1987).
54. H. Matsuoka, H. Tanaka, N. Iizuka, T. Hashimoto, N. Ise, Elastic scattering from cubic lattice systems with paracrystalline distortion. II. *Phys. Rev. B, Condens. Matter.* **41**, 3854–3856 (1990).
55. W. Zhou *et al.*, Preparation of calcium alginate/polyethylene glycol acrylate double network fiber with excellent properties by dynamic molding method. *Carbohydr. Polym.* **226**, 115277 (2019).
56. W. Zhou *et al.*, Sodium alginate-polyethylene glycol diacrylate based double network fiber: Rheological properties of fiber forming solution with semi-interpenetrating network structure. *Int. J. Biol. Macromol.* **142**, 535–544 (2020).
57. L. A. Hockaday *et al.*, Rapid 3D printing of anatomically accurate and mechanically heterogeneous aortic valve hydrogel scaffolds. *Biofabrication* **4**, 035005 (2012).
58. C. F. Guimarães, L. Gasperini, A. P. Marques, R. L. Reis, The stiffness of living tissues and its implications for tissue engineering. *Nat. Rev. Mater.* **5**, 351–370 (2020).
59. A. S. Hoffman, Hydrogels for biomedical applications. *Adv. Drug Deliv. Rev.* **64**, 18–23 (2012).
60. P. Treenate, P. Monvisade, M. Yamaguchi, Development of hydroxyethylacryl chitosan/alginate hydrogel films for biomedical application. *J. Polym. Res.* **21**, 1–12 (2014).
61. N. C. Hunt, A. M. Smith, U. Gbureck, R. M. Shelton, L. M. Grover, Encapsulation of fibroblasts causes accelerated alginate hydrogel degradation. *Acta Biomater.* **6**, 3649–3656 (2010).
62. Y. Jin, C. Liu, W. Chai, A. Compaan, Y. Huang, Self-supporting nanoclay as internal scaffold material for direct printing of soft hydrogel composite structures in air. *ACS Appl. Mater. Interfaces* **9**, 17456–17465 (2017).
63. B. Duan, L. A. Hockaday, E. Kapetanovic, K. H. Kang, J. T. Butcher, Stiffness and adhesivity control aortic valve interstitial cell behavior within hyaluronic acid based hydrogels. *Acta Biomater.* **9**, 7640–7650 (2013).
64. K. M. Mabry, R. L. Lawrence, K. S. Anseth, Dynamic stiffening of poly(ethylene glycol)-based hydrogels to direct valvular interstitial cell phenotype in a three-dimensional environment. *Biomaterials* **49**, 47–56 (2015).
65. N. Betancourt, X. Chen, Review of extrusion-based multi-material bioprinting processes. *Bioprinting* **25**, e00189 (2022).
66. S. Zheng, Z. Li, Z. Liu, The fast homogeneous diffusion of hydrogel under different stimuli. *Int. J. Mech. Sci.* **137**, 263–270 (2018).
67. S. Murdan, Electro-responsive drug delivery from hydrogels. *J. Control. Release* **92**, 1–17 (2003).
68. B. Duan, L. A. Hockaday, K. H. Kang, J. T. Butcher, 3D bioprinting of heterogeneous aortic valve conduits with alginate/gelatin hydrogels. *J. Biomed. Mater. Res. A* **101**, 1255–1264 (2013).
69. B. Duan, E. Kapetanovic, L. A. Hockaday, J. T. Butcher, Three-dimensional printed trileaflet valve conduits using biological hydrogels and human valve interstitial cells. *Acta Biomater.* **10**, 1836–1846 (2014).
70. C. Zhang *et al.*, Sacrificial scaffold-assisted direct ink writing of engineered aortic valve prostheses. *Biofabrication* **15**, 045015 (2023).
71. N. Valentin *et al.*, Direct ink writing to fabricate porous acetabular cups from titanium alloy. *Biodes. Manuf.* **6**, 121–135 (2023).
72. S. Boularaoui, G. Al Hussein, K. A. Khan, N. Christoforou, C. Stefanini, An overview of extrusion-based bioprinting with a focus on induced shear stress and its effect on cell viability. *Bioprinting* **20**, e00093 (2020).
73. M. Li, X. Tian, D. J. Schreyer, X. Chen, Effect of needle geometry on flow rate and cell damage in the dispensing-based biofabrication process. *Biotechnol. Prog.* **27**, 1777–1784 (2011).
74. X. B. Chen, M. G. Li, H. Ke, Modeling of the flow rate in the dispensing-based process for fabricating tissue scaffolds. *J. Manuf. Sci. Eng.* **130**, 021003 (2008).
75. J. Liu *et al.*, 3D printing of biomimetic multi-layered GelMA/nHA scaffold for osteochondral defect repair. *Mater. Des.* **171**, 107708 (2019).
76. P. Zhao *et al.*, Rapid printing of 3D porous scaffolds for breast reconstruction. *Biodes. Manuf.* **6**, 691–703 (2023).
77. A. Nadernezhad *et al.*, Nanocomposite bioinks based on agarose and 2D nanosilicates with tunable flow properties and bioactivity for 3D bioprinting. *ACS Appl. Bio Mater.* **2**, 796–806 (2019).